

TECHNICAL REPORT

Semiautomatic Extraction Algorithm for Images of the Ciliary Muscle

Chiu-Yen Kao*, Kathryn Richdale†, Loraine T. Sinnott*, Lauren E. Grillott‡, and Melissa D. Bailey§

Abstract

Purpose. To develop and evaluate a semiautomatic algorithm for segmentation and morphological assessment of the dimensions of the ciliary muscle in Visante Anterior Segment Optical Coherence Tomography images.

Methods. Geometric distortions in Visante images analyzed as binary files were assessed by imaging an optical flat and human donor tissue. The appropriate pixel/mm conversion factor to use for air ($n = 1$) was estimated by imaging calibration spheres. A semiautomatic algorithm was developed to extract the dimensions of the ciliary muscle from Visante images. Measurements were also made manually using Visante software calipers. Interclass correlation coefficients and Bland-Altman analyses were used to compare the methods. A multilevel model was fitted to estimate the variance of algorithm measurements that was due to differences within- and between-examiners in scleral spur selection vs. biological variability.

Results. The optical flat and the human donor tissue were imaged and appeared without geometric distortions in binary file format. Bland-Altman analyses revealed that caliper measurements tended to underestimate ciliary muscle thickness at 3 mm posterior to the scleral spur in subjects with the thickest ciliary muscles ($t = 3.6$, $p < 0.001$). The percent variance due to within- or between-examiner differences in scleral spur selection was found to be small (6%) when compared with the variance because of biological difference across subjects (80%). Using the mean of measurements from three images, achieved an estimated interclass correlation coefficient of 0.85.

Conclusions. The semiautomatic algorithm successfully segmented the ciliary muscle for further measurement. Using the algorithm to follow the scleral curvature to locate more posterior measurements is critical to avoid underestimating thickness measurements. This semiautomatic algorithm will allow for repeatable, efficient, and masked ciliary muscle measurements in large datasets.

(Optom Vis Sci 2011;88:1-●●●)

Key Words: optical coherence tomography, image segmentation, ciliary muscle, computational modeling

The traditional method for imaging the ciliary body in clinical practice and research is ultrasound biomicroscopy (UBM). A literature search in early 2010 revealed 341 publications in which a UBM was used to image the ciliary body in studies of tumors of the ciliary body,¹⁻⁴ accommodation,⁵ accommodating intraocular lenses,⁶ glaucoma,⁷ and the relationship between refractive error and ciliary body dimen-

sions.^{8,9} Despite the fact that >300 publications have used the UBM to image the ciliary body, there is a relative paucity of literature related to the development and function of the ciliary body throughout the human life span. In fact, the ciliary muscle is perhaps the only smooth muscle without an associated disease state; it is either an unusually robust organ or the discomfort, and invasive nature of viewing the ciliary muscle with the UBM has limited detection of ciliary muscle diseases and disorders.

Recently, the development of the Zeiss Visante Anterior Segment Optical Coherence Tomographer (OCT, Carl Zeiss Meditec, Dublin, CA) has allowed for non-contact imaging of the ciliary body. This is especially important for pediatric research.¹⁰ Pediatric studies of the relationship between refractive error and ciliary body dimensions¹⁰ and between accommodative microfluctuations and ciliary body dimensions¹¹ would not have been feasible using the UBM. In the future, the authors

*PhD

†OD, MS, FFAO

‡OD, MS

§OD, PhD, FFAO

Department of Mathematics and Mathematical Biosciences Institute, College of Mathematics and Physical Sciences (C-YK), and College of Optometry (KR, LTS, LEG, MDB), The Ohio State University, Columbus, Ohio.

Supplemental digital content is available for this article. Direct URL citations appear in the printed text and are provided in the HTML and PDF versions of this article on the journal's Web site (www.optvissci.com).

plan to use the Visante Anterior Segment OCT in studies of the relationship between refractive error and ciliary body dimensions, in studies of the ciliary body in accommodative dysfunction in children, and in studies of the ciliary body in developing presbyopia.

Although the Visante was not specifically designed for imaging the ciliary body or measuring its dimensions, there are a number of published studies showing that the Visante provides repeatable and valid measurements of central corneal thickness,^{12,13} crystalline lens thickness,¹⁴ and anterior chamber depth.^{12,13} In addition, Dada et al.¹³ reported that Visante Anterior Segment OCT images showed sharper definition of the scleral spur. Based on these data, one might expect that the Visante would also provide high-quality images of the ciliary body that would allow for repeatable and valid measurements of ciliary body dimensions; however, this topic has not been fully addressed in the literature.

As Westphal et al.¹⁵ have pointed out previously, OCT instruments are becoming valuable tools for imaging human tissue, but a raw image obtained from these instruments may be subject to distortions because of non-linear axial scanning, non-telecentric scanning, and lack of correction for the refractive properties of the tissue that is imaged. While the literature cited above suggests that the manufacturer has addressed these distortions when the Visante is used to image and measure the anterior segment, the Visante was not designed to image and measure the ciliary body. In measuring the ciliary body with the calipers in the Visante software in previous studies,^{10,11} we discovered several inadequacies of the calipers when used in ciliary body images that prompted us to begin analyzing a raw format of the images, i.e., binary files, in third-party software. Using a raw format of the images has, of course, necessitated evaluating distortions in the images. The first inadequacy we noted was that it is impossible for the examiner who acquired the images to make measurements in a masked fashion. Second, the calipers in the Visante software are straight lines, and in some

patients, the sclera is curved. When calipers are used to locate the desired measurement distance from the scleral spur, they cut across ciliary body rather than follow the curvature of the sclera (Fig. 1). In our previous studies using the calipers in the Visante software,^{10,11} we noted that some subjects had a flatter scleral curvature, whereas other subjects had a steeper scleral curvature. These scleral curvature differences could lead to an increased variability in the ciliary body thickness measurements, especially as measurements are made at an increasing distance from the scleral spur. Third, if one wants to make measurements of ciliary body thickness that are in the range of a physiologically accurate measurement, the Visante software is not programmed to apply an appropriate refractive index or scaling factor to the image of the sclera and ciliary body. Finally, measurements of the cross-sectional area cannot be made using tools available within the Visante software (Carl Zeiss Meditec, Dublin, CA) but may be critical to understanding changes in the ciliary body with presbyopia.

To address these inadequacies, a semiautomatic extraction algorithm was developed to objectively and accurately measure the dimensions of the ciliary body. The algorithm uses active contour models that have been successfully applied in the segmentation of many types of images.^{16–21} These models can produce sub-pixel accuracy of object boundaries, incorporate regional information for robust segmentation, and provide smooth and closed contours of the object of interest. Recently, a new active contour model based on a local binary fitting energy was proposed to segment magnetic resonance images with intensity inhomogeneity.^{22,23} Here, we extend the model to outline the boundary of the ciliary muscle. To avoid any image alteration created by the Visante software when generating a jpeg file, we use the raw images in the form of binary files that were exported from the Visante. The use of a raw image format, however, required that we also assess the raw images for distortions as described by Westphal et al.¹⁵

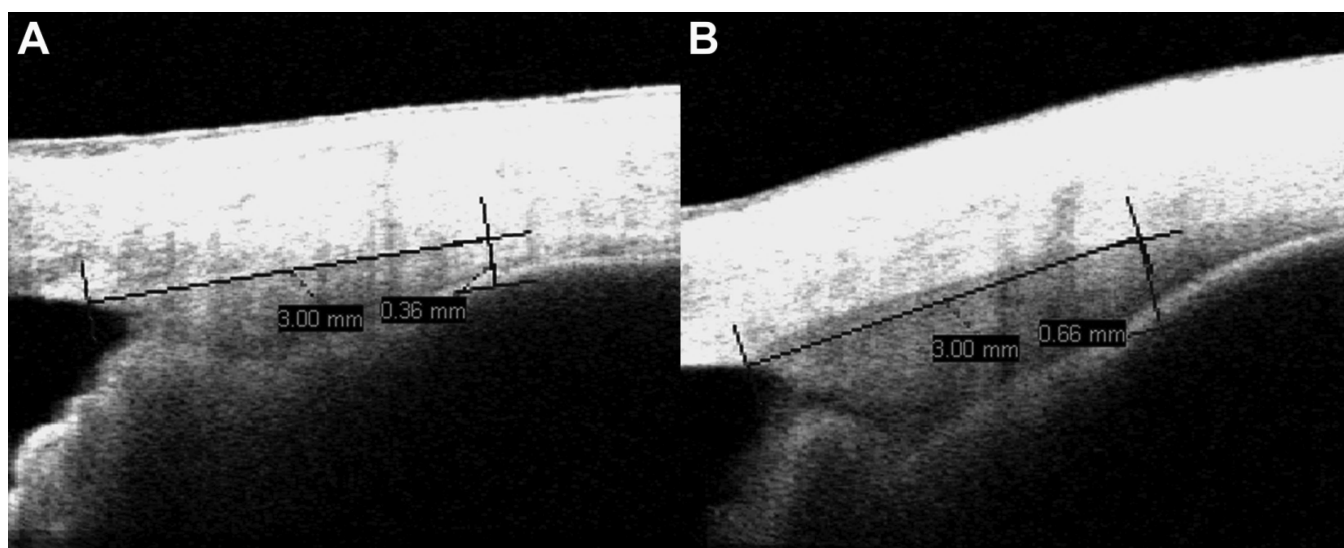


FIGURE 1.

Example images of the ciliary body obtained with the Zeiss Visante Anterior Segment OCT. (A) An image where the scleral curvature appears relatively flat, and the caliper used to align a measurement 3 mm posterior to the scleral spur follows the contour of the sclera rather closely. (B) An image where the scleral curvature appears somewhat steeper, and the caliper used to align a measurement 3 mm posterior to the scleral spur cuts across the ciliary muscle rather than following the contour of the sclera.

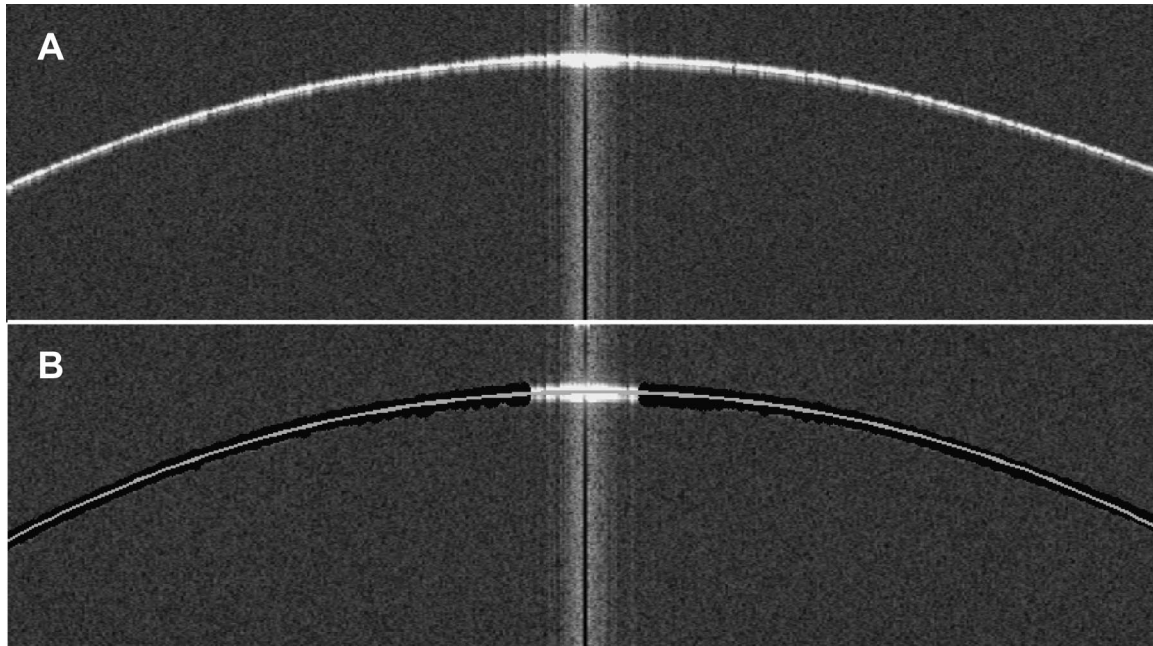


FIGURE 2.

(A) Image of a steel calibration sphere with radius 11.91 mm in enhanced high-resolution corneal mode. (B) An image of the 11.91 mm radius calibration sphere after identifying the pixels in the image of the sphere (black dots) and fitting a circle through a standard least square method (light gray line).

In summary, aims for this study were as follows.

1. To investigate and develop a correction for any image distortion in the binary files exported from the Visante Anterior Segment OCT by determining:
 - a. The appropriate pixel per mm conversion factor in Visante images for both air and the sclera/ciliary body;
 - b. The general fidelity and level of geometric and refractive distortions present in the raw images obtained with the Visante; and
2. To develop a semiautomatic algorithm for outlining and measuring the ciliary body in Visante images and assess the performance of the algorithm by determining:
 - a. The within- and between-examiner variability for (i) caliper measurements from the Visante analysis software; and (ii) the semiautomatic algorithm measurements;
 - b. The number of images needed per subject to provide acceptably repeatable algorithm measurement in future studies; and
 - c. The agreement between semiautomatic algorithm measurements and caliper measurements (Visante software).

With these study aims, we have demonstrated below that the binary files exported from the Visante provide renderings of the structure of human sclera and ciliary muscle that are free from geometric distortions and that the semiautomatic algorithm is capable of segmenting the ciliary muscle in Visante images and providing a repeatable measurement.

METHODS

Pixel per Millimeter Conversion Factor (Air)

To determine the correlation between pixel number and length, eight steel calibration spheres of various radii of curva-

ture (range, 5.995 to 11.91 mm) were mounted with a clamp and imaged with the Visante in a manner identical to imaging the ciliary body. The binary file for each calibration sphere image was imported into Matlab as a two-dimensional matrix of size 512×1280 (128 pixels per millimeter, per manufacturer's instructions). Fig. 2A is an image for a calibration sphere with radius 11.91 mm. Because the sphere contour appeared as a bright thin band and the "corneal reflex" at the center of the image also appeared as a bright thin band, pixels were selected for the curve fitting through a threshold detection procedure, i.e., if they had an intensity of more than 80% of the maximal intensity of the image and were located at least 64 pixels away from the center line of the image. These pixels are shown as black dots in Fig. 2B. The black dots were fitted with a circle (light gray line) through a standard least square method. The radius of the fitted sphere was determined in pixels.

The number of pixels in the radius of the fitted curve for each calibration sphere vs. the known radius of each calibration sphere in millimeters was plotted (Fig. 3). The slope of the fitting line of the eight calibration datasets was 132.35 pixels per millimeter. The difference between this value and the manufacturer's recommended conversion factor, 128 pixels per millimeter, represented an error of $<5\%$. Thus, we used 128 pixels per millimeter for analyzing the portions of the binary image files that were in air ($n = 1$).

Evaluation of Image Distortion in Binary Files

To evaluate the extent of geometric distortion in images, an optical flat (Edmund Optics, fused silica, $n = 1.458$, certified flat to within $\frac{1}{4}$ wavelength) was imaged with the Visante in a manner identical to imaging procedures described below for ciliary body imaging. Fig. 4 is an image of the optical flat in Enhanced High Resolution Corneal Mode. Note that the image appears to be flat,

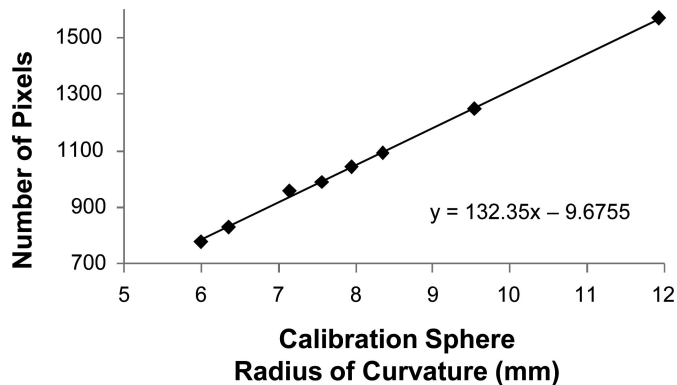


FIGURE 3.

A plot of the known radius of each of eight calibration spheres vs. the radius in pixels of the fitted curve from Visante images of each calibration sphere.

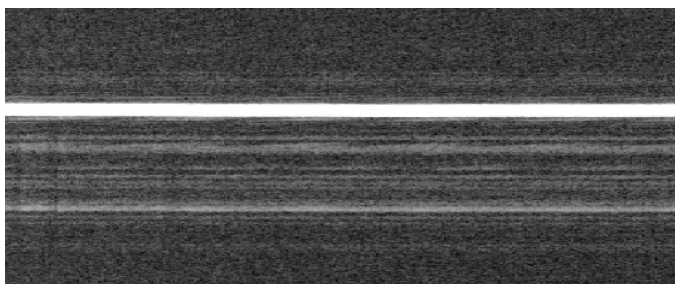


FIGURE 4.

Visante image of the front surface of an optical flat (bright white line) taken in Enhanced High-Resolution Corneal Mode. Note that there is no apparent warpage of curvature in the periphery of the image. The y-axis location of the optical flat within the image varied by only one to two pixels across the image.

with no distortion of curvature in the periphery of the image. When the binary file for this image was imported into Matlab, the y coordinates of the center of the reflection of the surface of the optical flat varied by only 1 to 2 pixels across the length of the image.

An additional experiment was conducted to evaluate the multiple distortions (geometric and refractive) of images of the sclera and ciliary body. Human eye tissue (right eye, 37-year-old, white male, fixed in 10% formalin) was obtained from the National Disease Research Interchange. A small section of sclera and ciliary muscle tissue (Fig. 5A) was imaged using both the Visante and digital photography. The anterior-posterior length of the tissue was selected such that the anterior and posterior cut ends of the tissue were visible within the lateral imaging view of the Visante in enhanced high-resolution corneal mode. Once the tissue had been sectioned from the globe, the iris tissue in the section stuck to the inner wall of the limbus/cornea rather than remaining suspended in what used to be the anterior chamber, so the iris was removed to make imaging and tracing (described below) easier. Then, the tissue was positioned on a piece of foam board such that the scleral wall was perpendicular to the surface of the board. The tissue was held in the perpendicular position with very thin sewing needles (Richard Hemming & Son, Large Eye Needles, Betweens Size 12, England). The sewing needles were positioned in the anterior chamber angle and at the posterior end of the scleral wall and ciliary body (Fig. 5A) so that they would not block the scanning

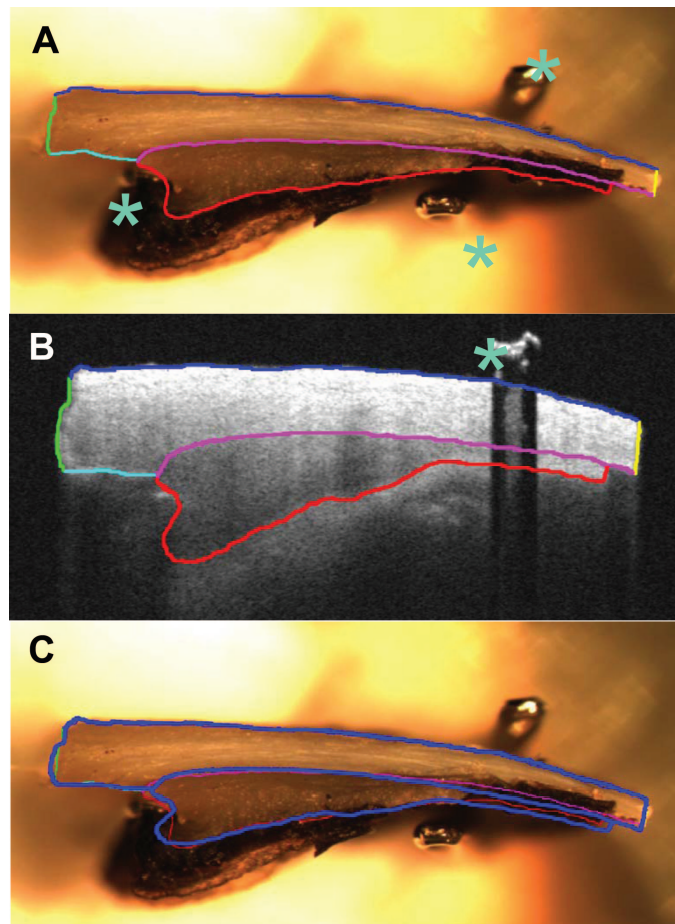


FIGURE 5.

A, A photograph of human donor sclera and ciliary body tissue after outlining the relevant structures in Photoshop. Asterisks denote the location of three sewing needles that were used to hold the tissue to a foam board. B, A Visante image of the same donor tissue that was also outlined in Photoshop. The asterisk denotes the location of a sewing needle on the outer scleral wall that is blocking the infrared scanning beam except for when the beam travels through the eye of the needle. (C) A photograph of the same tissue as in A after registration of the Visante image in B to the photograph in A. The blue outline represents the outline of the image in B after it has undergone an axial scan depth adjustment for the path length of the infrared light through the sclera and ciliary body. Note that the registration of the Visante image (blue line) very closely matches the photograph of the tissue.

beam of the Visante in the thicker, more anterior portion of the ciliary body.

In imaging the tissue with the Visante, it was important that the wall of the sclera be positioned perfectly orthogonal to the instrument's scanning beam. Otherwise the path length of the infrared light through the tissue would be artificially increased due to the tissue tilt, and subsequent registration of the Visante images with photographs of the tissue would be inaccurate. To appropriately position the tissue, the operator of the Visante was careful to have the foam board parallel to the floor; however, it was difficult to establish, from the operator's view point, if the scleral wall was rotated about the vertical axis during imaging. We discovered that if the eye of one sewing needle were placed flat against the scleral wall, the Visante would image through the eye of the needle only when the tissue was aligned orthogonally to the scanning beam in

that dimension. The shadow cast by the needle along the scleral wall is visible in Fig. 5B. Thus, tilt or turn about the horizontal axis was monitored by insuring the foam board was parallel to the floor and about the vertical axis by insuring the Visante was imaging through the eye of the needle. The scanning beam in the Visante appears as a visible horizontal line of light on the eye (or tissue) during imaging, and this horizontal line was always at the cut edge of the tissue that was furthest from the foam board. This meant the Visante was imaging the same portion of tissue that was photographed.

The same piece of tissue was also digitally photographed. The tissue was placed in front of the camera so that the cut edge, a cross-sectional view of the sclera and ciliary body, was visible. Photographs were taken only when the tissue was positioned so that the camera operator could not see down the wall of the sclera or the down the inner surface of the ciliary body, i.e., only the cross-section of tissue was visible. The only exception to this was at the most posterior end of the sclera/ciliary body. This portion of the tissue was the thinnest and it was difficult to get the wall of the sclera perpendicular to the foam board at this location; it tended to bend slightly (Fig. 5A). We accounted for this problem when completing the registration of the Visante images with the photographs by biasing the registration calculations to align the more anterior portions of the sclera/ciliary body where the tissue did not bend.

To facilitate registration of the photographs and the Visante images of the tissue, both were outlined in Photoshop (Adobe, San Jose, CA). In the Visante images (Fig. 5B), the inner (pink line) and outer borders (blue line) and the cut ends (green and yellow lines) of the sclera were traced, and the ciliary body was also traced along the heavier white boundary in the image that was created by the ciliary pigmented epithelium (red line). In the photographs (Fig. 5A), the sclera was traced in an identical manner as in the Visante images, and the ciliary body was also traced along the ciliary pigmented epithelium because it was assumed that the highly pigmented processes and folds of the pars plicata would not be visible in Visante images.

The Visante images were then registered to photographs using rigid transformation which includes translation, rotation, and uniform scaling.²⁴ We first registered the outer surface of the sclera and the cut ends of the sclera (blue, yellow, and green lines) because the infrared scanning beam in these portions of the image would be traveling in air. Before entering the tissue, the index of refraction should be $n = 1.0$. Registration of the entire image to align these edges accounted for simple magnification differences between the Visante images and the photograph, i.e., differences that were not due to the path length of the infrared light through the sclera and ciliary body. After these lines were registered, one single adjustment in the y dimension of the image, i.e., the axial scan depth of the image, was made to align the turquoise curves. Alignment of the turquoise lines, in turn, was capable of providing very close alignment of the pink and red curves (Fig. 5C) without any additional adjustments, i.e., the entire width of the image was registered with only a refractive adjustment and no geometric adjustments for distortion were needed. This procedure was repeated with 16 different pairs of photographs and Visante images of the tissue. The mean \pm standard deviation (SD) adjustment along the axial scan depth that was required to register the scleral and ciliary body in the image pairs was 1.5586 ± 0.05 , i.e., the index of

refraction for the infrared light traveling through the sclera and ciliary body fixed in 10% formalin was established at $n = 1.56$. Fig. 5C shows the outline of the sclera and ciliary body from a Visante image (blue lines) after it has an appropriate refractive index applied to the scleral and ciliary body areas of the image ($n = 1.56$). Note that a single refractive index can be applied to create an acceptable image registration for both the inner scleral wall and the ciliary pigmented epithelium (Fig. 5C). Previous publications have reported the index of refraction or scaling factor for rabbit sclera and ciliary body to be 1.41 and 1.38, respectively.^{25,26} Bovine muscle tissue and human cardiac muscle were also reported to have a refractive index of 1.38.^{27,28} The slightly higher value reported here ($n = 1.56$) may be due to fixation of the tissue or slight tilting of the tissue during imaging with the Visante. Nonetheless, the imaging of the optical flat and the tissue registration process demonstrated that the binary files from the Visante provide images without geometric distortions and that the refractive indices of human sclera and ciliary muscle are probably very close to each other and close to what has been reported for the rabbit.

Semiautomatic Algorithm Development and Performance

Subjects

A cross-sectional study of 26 subjects (21 female) between the ages of 19 and 40 years (mean \pm SD = 25.3 ± 5.0 years) was conducted. The mean \pm SD spherical equivalent refractive error was -3.39 ± 3.4 D (range, -11.03 to $+3.13$ D). Subjects were required to have best spectacle-corrected visual acuity better than 20/40 in each eye to assure proper target fixation during measurement, and all subjects were free of ocular disease other than refractive error. An effort was made to recruit subjects with a wide range of refractive error. The Ohio State University's Biomedical Sciences Institutional Review Board, in accordance with the tenets of the Declaration of Helsinki, approved the study protocol. Subjects were educated on the purpose of the study, and informed consent was obtained from each subject before beginning the study. Subjects were recruited using posters and e-mail announcements at The Ohio State University.

Testing Procedures

Refractive error and ciliary body thickness measurements were made under cycloplegic conditions on right eyes only. One drop of 0.5% proparacaine hydrochloride ophthalmic solution was given, followed by 2 drops of 1% tropicamide ophthalmic solution administered 5-min apart. Testing was completed 30 min after the first drop of tropicamide. Refractive error was measured with a Grand Seiko autorefractor (Grand Seiko Co., Ltd., Hiroshima, Japan). The mean spherical equivalent from five measurements was reported.

The nasal ciliary body of each subject was imaged through the sclera while the subject viewed an external target. Images were obtained in Enhanced High Resolution Corneal Mode, a high-resolution imaging mode available with the Visante 2.0 software. All images were obtained by the same examiner (LEE). Six images of the ciliary body were obtained, and the subject was realigned between each measurement.

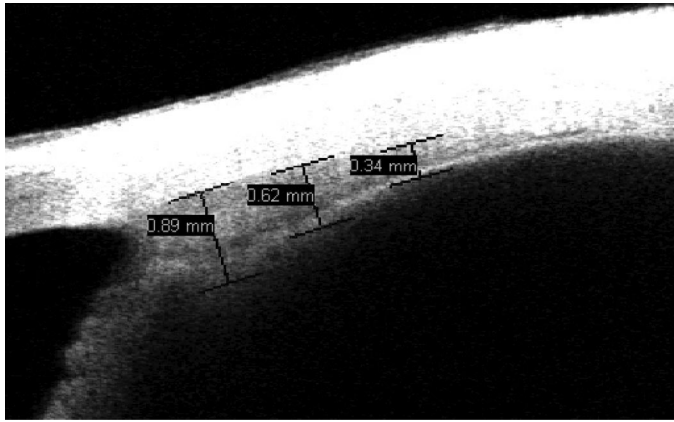


FIGURE 6.

An image of the ciliary body showing all three caliper measurements, i.e., at 1 mm (CBT1), 2 mm (CBT2), and 3 mm (CBT3) posterior to the scleral spur. The caliper measurements were created with the Visante software.

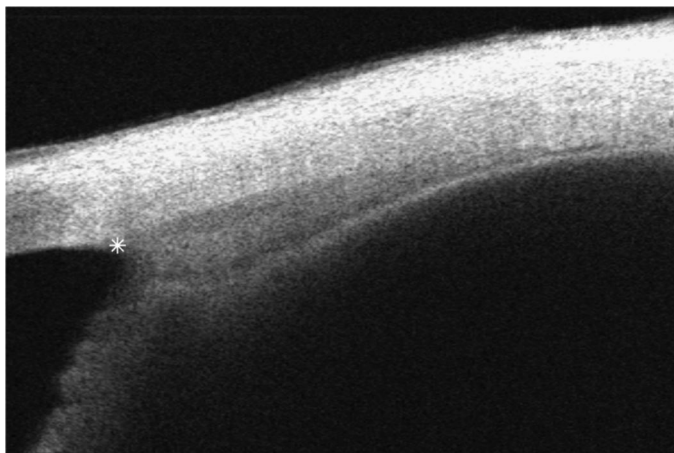


FIGURE 7.

An example of an image of the ciliary body that was exported from the Visante as a binary file. The location of the scleral spur is indicated in the image with a white asterisk. The image was cropped to include the area 1 mm to the left and 6 mm to the right of the scleral spur.

Ciliary Body Measurements with Calipers

When images were measured with the calipers, a uniform refractive index of 1.0 was applied to the entire image by editing the image so that both corneal surface lines were flat and at the very bottom of the image. Although there are estimates of the appropriate refractive index for the sclera/ciliary body in the published literature,^{25,26} it is not currently an option to incorporate this refractive index into measurements made with the calipers in the Visante software. Thickness measurements were obtained at 1 mm, 2 mm, and 3 mm posterior to the sclera spur (Fig. 6) using calipers in the Visante software as previously described.¹⁰ Thickness measurements were completed on each of the six images by one experienced examiner (MDB) and one inexperienced examiner (KR). Because the images and all other study measurements were acquired by a different examiner (LEE), both examiners making measurements with calipers were masked to the refractive error status of the study subjects. The data were entered into an Excel spreadsheet.

Semiautomatic Extraction Algorithm

Preparing the Images for Analysis: Region of Interest and Down-Sampling

For the semiautomatic algorithm, raw images (refractive index of 1.0) were exported as binary files (.bin) using the Visante OCT Image Exporter software. The images were then imported into Matlab for extraction with the semiautomatic algorithm as described in detail below. The raw images acquired with the Visante were gray-scale images of size 512×1024 pixels (4 cm by 10 cm) (Fig. 7). After discussions with engineers at Zeiss who work with the Visante, the images were resized to 512×1280 pixels (1:2.5, and 128 pixels per mm) so that the images could be visualized in the original aspect ratio. In Matlab, resizing is implemented as $B = \text{imresize}(A, (512, 1280), \text{bicubic})$, which resizes image A to image B (512×1280 pixels) by applying a low-pass filter before the bi-cubic interpolation to reduce aliasing.

The first step, and the only step requiring human input into the image analysis process, was to manually select the location of the scleral spur. One experienced examiner (MDB) and one trained examiner (KR) visually inspected the image and clicked on the scleral spur (Fig. 7, asterisk). In a previous publication from this laboratory, the mean (\pm SD) distance of the location of three selections of the scleral spur was $3.98 (\pm 2.89)$ pixels from the mean location of the scleral spur.¹⁰ Because of this minor variation in the selection of the scleral spur, the scleral spur was manually selected three times for each image, and the mean coordinates of the three selections was used as the final location of the scleral spur in subsequent processing. This process was then repeated by both examiners a second time so that the within-examiner variance could be determined.

The horizontal dimension of the image was cropped to include the area of primary interest, i.e., the ciliary body, at 128 pixels to the left and 768 pixels to the right of the scleral spur. The cropped image dimensions were 512×896 pixels (Fig. 7). Because Visante images are high-resolution, processing the original raw images is time intensive. The time required for analysis was reduced by down-sampling the images to one fourth their original size before analysis. In Matlab, this was implemented by using $B = \text{imresize}(A, 1/4, \text{bicubic})$.

Region-Scalable Image Segmentation Algorithm

Step 1: Extracting the Ocular Structure from the Background

The first step in the region-scalable image segmentation algorithm was to delineate the ocular structures from the background. This was necessary so that the otherwise dark ciliary body area could be extracted from the other, lighter, ocular structures such as the sclera. The process of delineation is illustrated by the white outlines in Fig. 8. A region-based segmentation model, that used the intensity information in local regions at a controllable scale, was used. The function used in step 1 is provided in Appendix A (available at <http://links.lww.com/OPX/A39>). The parenthetical remarks in this section refer to notation used in the Appendix.

The delineation process began by generating an approximation of the shape of the ocular structures (curve = Γ) to serve as a

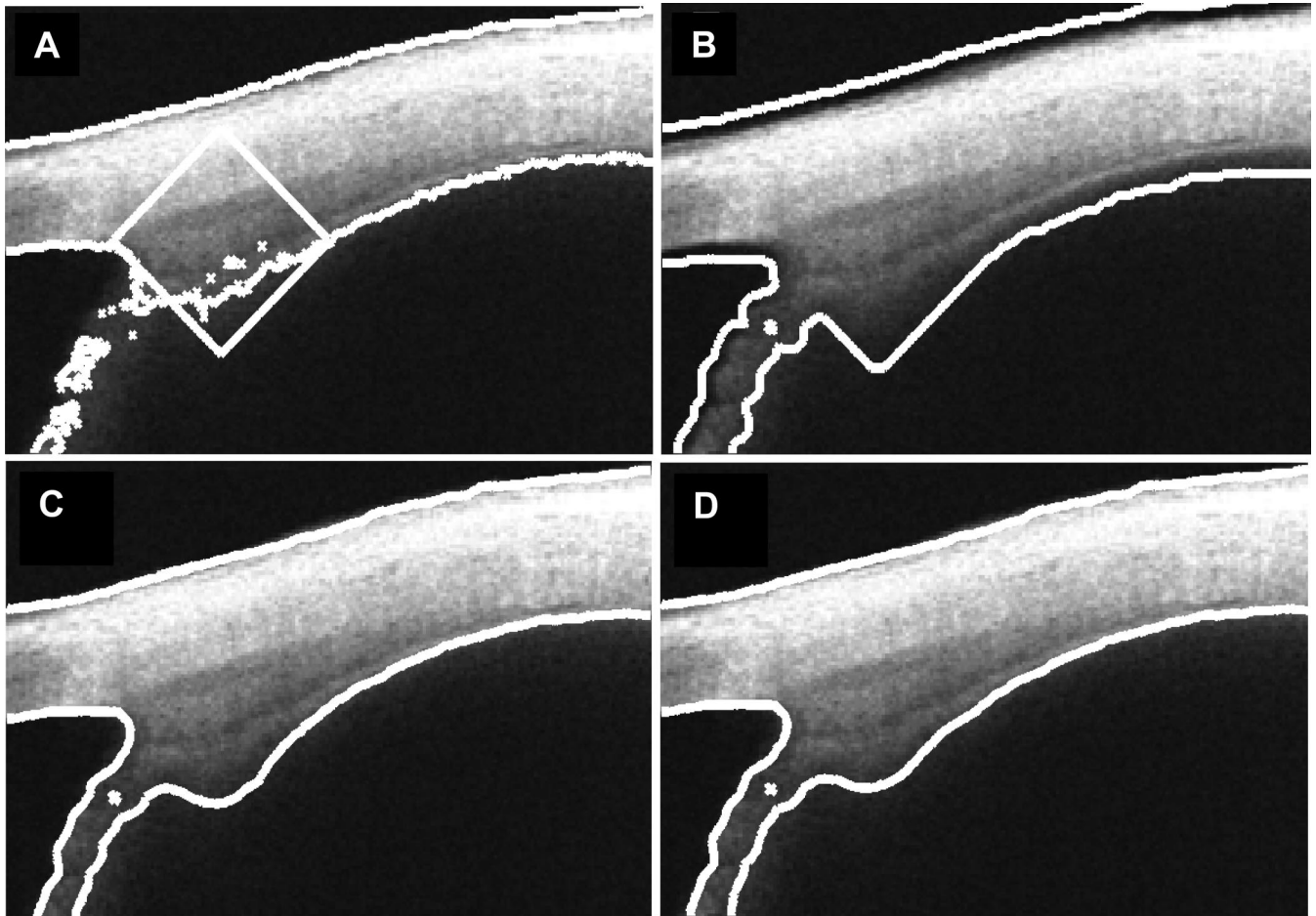


FIGURE 8.

A, An outline of the regions where the pixel intensity was greater than the mean. The region of the ciliary body apex, which often appeared darker than the rest of the ciliary body, was also considered by including the region in the white diamond shape. B, An outline of the dilated region with a rolling ball structuring element. C, An outline of ciliary body in white which was extracted by a region-scalable fitting segmentation model at the 25th iteration. D, An outline of ciliary body in white which was extracted by a region-scalable fitting segmentation model at 100th iteration.

starting point (which was represented as $\{X|\phi(X) = 0\}$). A simple way to generate the initial approximation was to find the region where the pixel intensity was greater than the mean; however, the boundary of this region was usually not smooth and often contained multiple subregions of pixel intensity (Fig. 8A). Furthermore, the region near the apex of the ciliary body was darker and usually was not identified by this thresholding technique. Thus, we include a diamond shape with 256 pixels in diagonal direction. Dilating the union of diamond shape region and the thresholding region with a rolling ball with a 5 pixel radius gave a better initial approximation of the outline (Fig. 8B). From this initial outline, the outline of the ocular structures evolved according to the model described in Appendix A and approached the boundary of the sclera and ciliary body as shown in Fig. 8C, D. The final outline is depicted in Fig. 8D.

Step 2: Extracting the Ciliary Body from the Ocular Structures

An approximation of the initial contour of the ciliary body (Fig. 9) was based on the histological data from the literature, indicating that the ciliary body was usually 4 to 6 mm long and 1 to 2 mm

wide at the point of greatest thickness.^{29,30} In Fig. 9A, p1 is the location of the manually selected scleral spur (described above). The second and third points (p2 and p3) were automatically selected by the algorithm on the lower branch of the red curve, 1.2 mm and 6 mm from the sclera spur in the horizontal direction, respectively. A point 0.5 mm above a line from p1 to p3 and half way between p1 and p3 served as the fourth point (p4). A parabola was constructed passing through p1, p4, and p3. This generated a reasonable guess of the upper boundary of the ciliary body. Connecting all the points created an initial closed contour approximation for the outline of the ciliary body (Fig. 9A).

Instead of considering the whole image domain, Ω (Fig. 7), only the energy^{21,22} defined on the region Ω_1 inside of the red curve (Fig. 9) was considered (Appendix B—available at <http://links.lww.com/OPX/A40>). When the energy was minimized,^{21,22} the curve stopped at the boundary of ciliary body/sclera. The contour of the ciliary body was then fine-tuned by repeating the algorithm on the high-resolution images, i.e., the original image before down-sampling, for a few time steps until it converged (Fig. 9B). We then applied an index of refraction of 1.41 to the region of the sclera and an index of refraction of 1.38 to the region of the ciliary body to shrink that portion of the image in

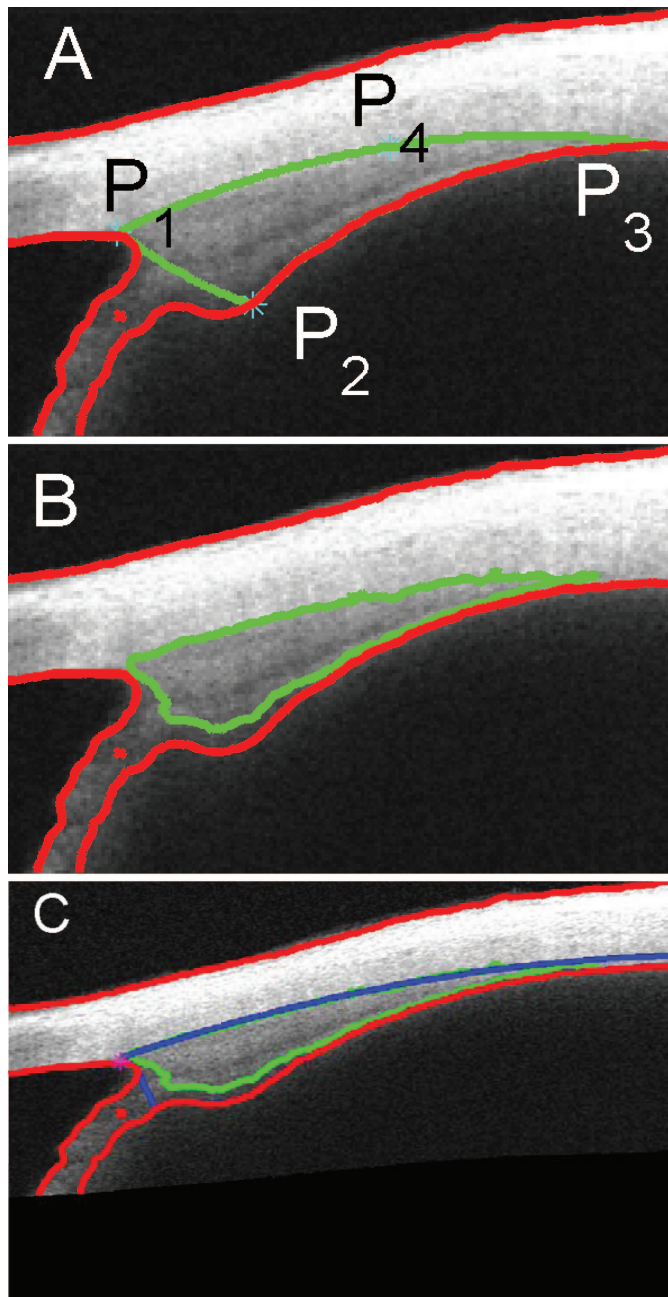


FIGURE 9.

A, The initial guess contour (green contour) for the ciliary body. B, The green curve shows the outline of ciliary body which was extracted by a region-scalable fitting segmentation model at 25th iteration. C, The final result of algorithm was shown in green and the fitting outline of ciliary body is shown in blue.

the y dimension only so that it represented an appropriate axial scan depth for subsequent measurements. A least squares method was used to fit a parabola to the upper contour of the green curve. The region of ciliary body was segmented by selecting the region below the parabola (p1-p4-p3) that was inside the outline of the sclera and ciliary body (red line). When a segment of the iris was visible in the images, it was removed by following the curve below scleral spur from p1 to p2. The final result of the algorithm is shown in blue in Fig. 9C. Note that the sclera and ciliary body sections of the image in Fig. 9C have

been adjusted to a refractive index of $n = 1.41$ and 1.38 , respectively, and that this region is noticeably thinner than before this refractive index is applied (Fig. 9B).

For analyses described below that required comparison of the algorithm to caliper measurements from the Visante software, we were unable to apply an appropriate refractive index to the area of the sclera and ciliary body because that is not an option available within the Visante software. So for the purposes of those algorithm-to-caliper comparisons in this article, we also obtained algorithm thickness measurements with a refractive index of 1.0 applied to the entire image.

Ciliary Body Measurements with Semiautomatic Extraction Algorithm

Based on the final ciliary body outline in Fig. 9C, thickness measurements were then obtained at 1 mm, 2 mm, and 3 mm (CBT1, CBT2, and CBT3) posterior to the scleral spur (Fig. 10). In addition, the thickest measurement of the ciliary body (CBTmax) was identified. The cross-sectional areas of portions of the first 3 millimeters of the ciliary body (CBA1, CBA2, and CBA3) were also measured. Measurements were made by counting the pixels in each portion and multiplying by the image resolution (1 mm = 128 pixels). These measurement points were chosen for this initial investigation, but once the ciliary body is outlined, it is possible to obtain ciliary body or scleral measurements at any location with this algorithm.

Statistical Analyses

Caliper and Algorithm Measurement Variability

As described above, thickness measurements, CBT1, CBT2, and CBT3 were made using both the algorithm and the Visante software calipers. Measurements of the thickest part of the ciliary body (CBTmax) and of the cross-sectional areas for the first 1 mm (CBA1), 2 mm (CBA2), and 3 mm (CBA3) of the ciliary body

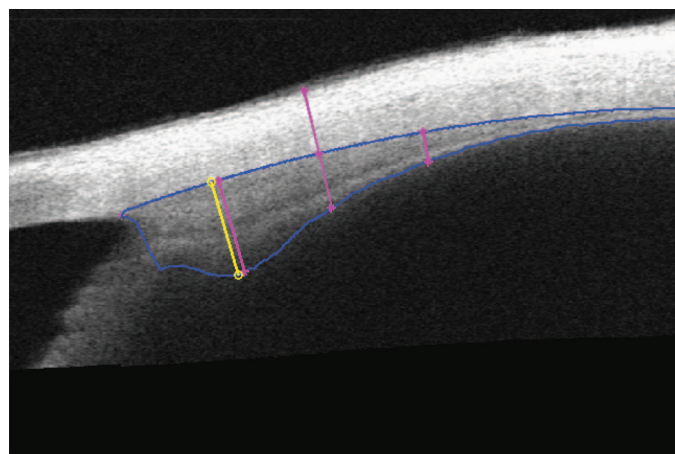


FIGURE 10.

Thickness measurements (pink lines) of the ciliary body and sclera can be obtained from the final outlines of the ciliary body and sclera. The point of maximum thickness is shown in yellow. Cross-sectional area measurements or scleral thickness measurements can also be obtained from the outlined areas.

were only made with the algorithm. For each subject, measurements were made on each of six images.

Bland-Altman analyses³¹ were used to assess the variability in the ciliary body measurements. Statistics from a Bland-Altman analysis indicate how repeatable a measure is in absolute terms. The mean of the differences between the repeated measurements characterizes the bias in measurement because of drift in the measurements over time or examiner differences. A one-sample t-test was used to test whether the mean of the differences was 0. The mean of the differences and its SD were used to construct 95% limits of agreement (LoA) [mean \pm (1.96 \times SD)]. The LoA characterize the expected differences between repeated measurements. They estimate the boundaries within which 95% of the differences should fall. The coefficient of repeatability (1.96 \times SD of the differences) was also calculated. The difference between the two measurements vs. the mean of the two measurements was graphed and visually inspected to determine if the repeatability of the measurement was related to the magnitude of the measurement. The following Bland-Altman comparisons were completed:

1. Evaluation of the repeatability of caliper and algorithm measurements
2. Comparison of caliper measurements taken from different examiners
3. Comparison of caliper and algorithm measurements
4. Comparison of simulated and examiner caliper measurements

Additionally, we sought to determine how within- and between-examiner differences in selecting the scleral spur would impact ciliary body thickness measurements made by the algorithm. The input to the algorithm is an image of the ciliary body. Factors that result in variability in the algorithm's measurements are the biological variability of the image's source (i.e., differences between subjects), the alignment during acquisition of each image, and the selection of the scleral spur within each image by an examiner. To assess the relative importance of the various sources of variability we fitted the following model:

$$CBT_{ijkl} = \mu + \text{subject}_i + \text{image}_{ij} + \text{examiner}_{ijk} + \text{error}_{ijkl}$$

CBT_{ijkl} is the thickness measure derived from the j th image taken for subject i using the l th scleral spur selection by examiner k . μ is the population mean of the ciliary body thickness measurement, subject_i is subject i 's deviation from the population mean because of biological variability, image_{ij} is the deviation from subject i 's measure because of variation in acquisition of individual images of the ciliary body, examiner_{ijk} is the deviation in the j th image from subject i because of bias in examiner k 's selection of the scleral spur for the image, and error_{ijkl} is random deviation from this bias for examiner k . subject_i , image_{ij} , and examiner_{ijk} were fitted as random effects and their variances estimated. For each CBT measurement, we present the percent of total variation in the measurement that is attributable to each factor. The sum of the percent for examiner and error provide the percent of total variation because of scleral spur selection. All modeling was done in SAS (SAS Institute Inc., Cary, NC) using the MIXED procedure.

The Number of Images Needed for Acceptable Repeatability

Interclass Correlation Coefficients (ICC) estimates were computed using parameters from the fitting of another random effects model, following a method outlined in Cox and Solomon.³² For a variable y (example, CBT2), the j^{th} measurement for subject i was modeled as follows.

$$y_{ij} = \mu + \epsilon_{ij}$$

In the model, μ is the population mean of the measurement and ϵ was the deviation from the mean of subject i 's j th measure. The deviation from the mean (ϵ) was decomposed into a deviation because of biological variability between subjects (δ_i) and within-subject measurement error (ξ_{ij}). This decomposition led to the following multilevel representation of y :

$$y_{ij} = \mu + \delta_i + \xi_{ij} \quad (1)$$

A metric of measurement repeatability is the ICC, which is the portion of overall score variance (given by the sum of the variances of δ and ξ) that is due to between-subject variance (given by the variance of δ). To compute this proportion, we fitted Eq. 1 using the SAS procedure MIXED. The procedure provided estimates of total and between subject variance.

We then computed estimates of what would happen if a measurement was a composite of multiple measurements of the variable on the same occasion. To obtain these estimates, we made use of the results from the fitting of Eq. 1. If z is the mean of n measures of y , the variance of z is the sum of the variance of δ and the variance of ξ divided by n .

The use of a mean has no effect on biological variability, but decreases within-subject variability by a factor of n , making total variability the sum of the variance of δ and the variance of ξ divided by n . We used the estimates from the SAS MIXED procedure for the variance of δ and ξ , adjusting estimates of total variability for $n = 1$ to 8 by using the sum of the variance of δ and the variance of ξ divided by n , to generate the data for the curves presented in the results.

The ICC was estimated for all thickness and area measurements. A higher ICC indicates a more consistent measurement. With higher ICC, the nuisance of measurement error within an individual is less likely to result in an error in the estimate of his relative ranking within the population. There is no consensus on what is an adequate ICC (range, 0 to 1). Nunnally and Bernstein³³ suggests that values >0.80 are adequate for research tools.

RESULTS

Semiautomatic Algorithm Extraction

The semiautomatic algorithm was able to successfully outline the ciliary body allowing for further morphological study. In our experience, the outlining procedure only failed on images where there were shadows because of eye lashes, on poor quality images because of eye movement, or when images were very tilted from poor subject alignment. The algorithm was successful in all images included in this report, as all were aligned appropriately and free of shadows or eye movements. The thickness and cross-sectional area

of the ciliary body were automatically measured at several points. Summary statistics for the ciliary body variables are presented in Table 1.

Caliper and Algorithm Measurement Variability

Results of the between-image repeatability analyses are presented in Table 2. For both the calipers and the algorithm, the first and sixth images were compared. Visual inspection of the difference vs. mean plots for the various algorithm thickness and area measurements did not reveal any relationship between the repeatability of a measurement and the magnitude of the measurement. The coefficient of repeatability, an indicator of measurement variability, was comparable across all variables,

TABLE 1.

Mean and SD of ciliary body thickness and cross-sectional area measurements for the caliper and algorithm measurement methods across all subjects

Measurement	Experienced examiner caliper measurements		Algorithm (refractive index, n = 1.00)		Algorithm (refractive index, n = 1.38)	
	Mean	SD	Mean	SD	Mean	SD
CBT1 (mm)	1.12	0.11	1.15	0.09	0.92	0.09
CBT2 (mm)	0.72	0.13	0.78	0.13	0.61	0.12
CBT3 (mm)	0.42	0.09	0.46	0.12	0.32	0.09
CBTmax (mm)	NA	NA	1.17	0.09	0.96	0.09
CBA1 (mm ²)	NA	NA	0.76	0.11	0.77	0.11
CBA2 (mm ²)	NA	NA	0.89	0.08	0.71	0.09
CBA3 (mm ²)	NA	NA	0.56	0.12	0.41	0.10

Algorithm measurements with a refractive index of n = 1 and n = 1.38 applied to the area of the sclera and ciliary body are both shown to allow for comparison with the caliper measurements (refractive index, n = 1).

NA, not available for this measurement method.

TABLE 2.

Bland-Altman analyses of the repeatability of single ciliary body measurements made by an examiner and with the algorithm (difference = last of the six measurements – first of the six measurements)

Measurement	Mean of the differences	SD of the differences	95% Limits of agreement		Coefficient of repeatability
			Lower bound	Upper bound	
Experienced examiner calipers					
CBT1 (mm)	-0.02	0.10	-0.21	0.18	0.19
CBT2 (mm)	-0.04	0.09	-0.22	0.14	0.18
CBT3 (mm)	-0.02	0.06	-0.15	0.11	0.13
Semiautomatic algorithm					
CBT1 (mm)	0.01	0.06	-0.11	0.13	0.12
CBT2 (mm)	-0.02	0.07	-0.15	0.11	0.13
CBT3 (mm)	-0.02	0.05	-0.12	0.08	0.10
CBTmax (mm)	0.01	0.08	-0.15	0.18	0.16
CBA1 (mm ²)	0.04	0.08	-0.12	0.20	0.16
CBA2 (mm ²)	-0.01	0.05	-0.11	0.08	0.10
CBA3 (mm ²)	-0.02	0.05	-0.12	0.07	0.09

ranging from 0.09 to 0.19 mm. For some of the calipers and the algorithm measurements, the sixth image's measurements tended to be smaller than the first image's measurement, although the magnitude of the means of the differences was small compared with the magnitude of the measurement. None of the means of the differences were statistically different from 0 after adjusting for multiple comparisons.

The between-examiner comparisons of the caliper measurements are shown in Table 3. Visual inspection of Bland-Altman difference vs. mean plots did not reveal any relationship between the magnitude of the measurement and the examiner agreement. The coefficient of repeatability was comparable across all variables. The experienced examiner made slightly thicker measurements at CBT1 ($t = 5.7$, $p < 0.0001$), and the inexperienced examiner made slightly thicker measurements at CBT3 ($t = 3.2$, $p = 0.004$). The magnitude, however, of the means of the differences between examiners is small compared with the magnitude of the measurements (CBT1: -0.06 mm vs. 1.12 mm and CBT3: 0.03 mm vs. 0.42 mm, respectively).

To further assess the performance of the algorithm, we completed an analysis to determine the percent of total variance in ciliary body thickness measurements that is attributable to each of the potential sources of variability (Table 4). The variance attributable to differences across subjects, i.e., variance because of biological variability, was ~80% for all three thickness measurements. Overall, the percent of variation that was attributable to differences between two examiner's scleral spur selections was about the same size as that variability because of scleral spur selection on different occasions by the same examiner (range, 1.5 or 3.8%), and this variability is very small when compared with the variability because of biological differences (~80%) or differences in image acquisition (~15%).

The Number of Images Needed for Acceptable Repeatability

The analysis in Table 4 shows that ~80% of the variability of the algorithm measurements is due to biological variability. The

TABLE 3.

Bland-Altman analyses of the agreement between the caliper measurements of the ciliary body made by the two different examiners (difference = inexperienced examiner – experienced examiner)

Measurement (mm)	Mean of the differences	SD of the differences	95% Limits of agreement		Coefficient of repeatability
			Mean lower bound	Mean upper bound	
CBT1	-0.06 ^a	0.08	-0.22	0.10	0.16
CBT2	0.01	0.08	-0.14	0.16	0.15
CBT3	0.03 ^b	0.06	-0.08	0.13	0.11

^at = -5.7, p < 0.0001.

^bt = 3.2, p = 0.004.

TABLE 4.

Percent of total variance attributable to the each potential sources of variability in the execution of the algorithm

Measurement location	Potential sources of variability (%)			
	Biological/inter-subject	Image acquisition	Between-examiners	Within-examiner
CBT1	82.3	12.5	1.5	3.8
CBT2	79.4	15.6	1.2	3.7
CBT3	79.6	14.9	2.7	2.9

Within-examiner variability can be interpreted as the variability associated with an examiner selecting the scleral spur location on two separate occasions and the between-examiner variability is the variability attributable to the differences in the scleral spur selection of two different examiners.

remaining 20%, because of positioning during image acquisition and within- and between-examiner differences, can be reduced by using the mean of multiple measurements. Fig. 11 illustrates the estimated increase in ICC if multiple images from the same subject are measured with the algorithm and the mean of those multiple measurements are used. If three images are used instead of one, all the ciliary body measurements have an estimated ICC >0.85.

Caliper and Algorithm Measurement Agreement

Table 5 is a summary of algorithm measurements compared with caliper measurements made by an experienced examiner. For all thickness measurements, the algorithm provided on average a slightly larger estimate of thickness than the caliper measurement. (Note that a refractive index of n = 1 was applied to the images used for both caliper and algorithm measurements because it is not possible to apply an appropriate refractive index to the ciliary body in the Visante software.) Visual inspection of Bland-Altman plots for CBT1 and CBT2 did not reveal any relationship between the difference in the measurements and the magnitude of the measurements. For CBT3, however, there was a trend. The algorithm provided thickness measurements that were increasingly thicker than the caliper measurements as the thickness of the ciliary body increased (Fig. 12).

It was expected that the algorithm measurements might be larger than the caliper measurements on average because the calipers cut across the ciliary muscle instead of following the scleral curvature (Fig. 1). A trend in the difference between the algorithm and caliper measurement was, however, unexpected and suggested that the problem depicted in Fig. 1B may become more pronounced in subjects with a thicker ciliary body. It was also possible,

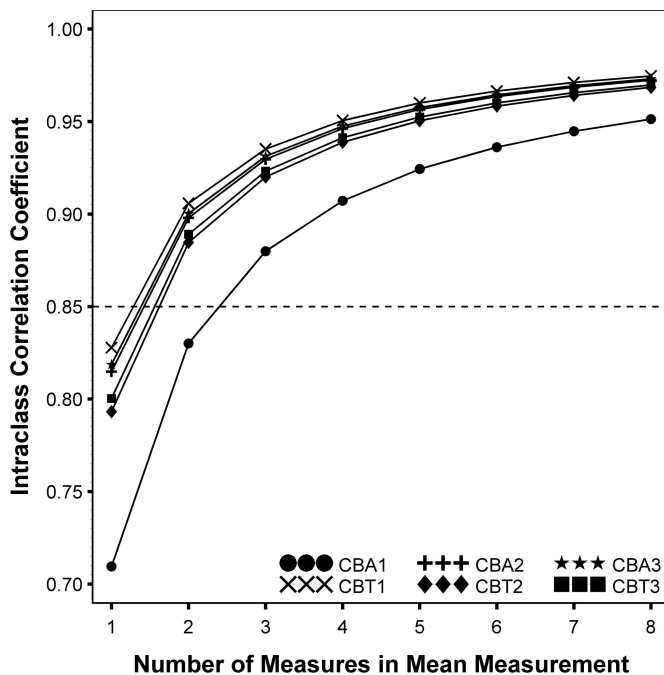


FIGURE 11.

An analysis for estimating the number of images needed to provide acceptably repeatable measurements of ciliary body dimensions using the semiautomatic algorithm. Interclass correlation (ICC) values for ciliary body measurements as a function of the number of measurements used to provide a mean measurement for a subject are shown. Using the mean of measurements from three images of the ciliary body would achieve the precision of a measurement with an ICC of at least 0.85 for all measurements, whereas using a single measurement from a session would only provide an ICC ranging from 0.71 to 0.83.

TABLE 5.

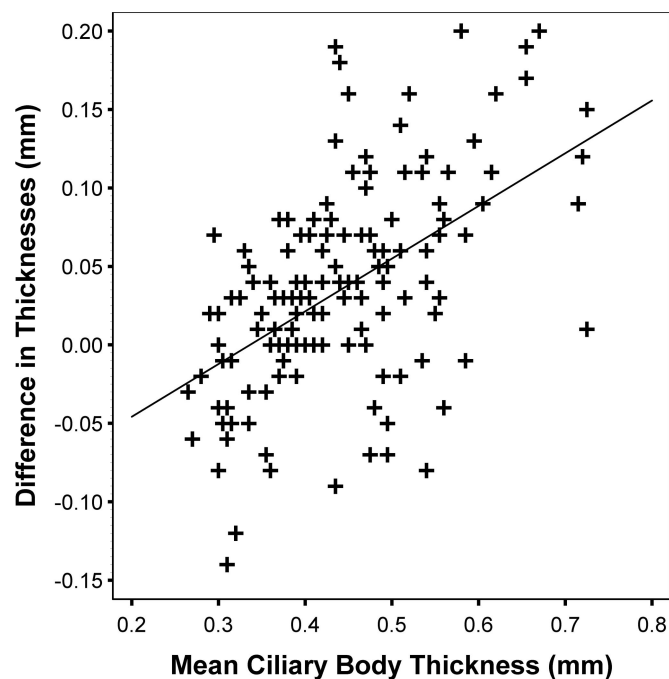
Bland-Altman analyses of the agreement between the semiautomatic algorithm and caliper measurements of the ciliary body (difference = algorithm measurements – experienced examiner caliper measurements)

Measurement (mm)	Mean of the differences	SD of the differences	95% Limits of agreement		Coefficient of repeatability
			Lower bound	Upper bound	
CBT1	0.03	0.13	-0.22	0.27	0.25
CBT2	0.06 ^a	0.09	-0.12	0.23	0.18
CBT3	0.03 ^b	0.07	NA	NA	0.13

^at = 5.9, p < 0.0001.

^bt = 3.6, p < 0.001.

NA, not applicable, the mean of the measurements was related to the difference between the measurements.

**FIGURE 12.**

A Bland-Altman difference vs. mean plot of the agreement between measurements made with the semiautomatic algorithm and the experienced examiner's caliper measurements at CBT3. The difference is related to the mean such that subjects with thicker ciliary bodies have a thicker measurements when the semiautomatic algorithm is used and thinner measurements when calipers in the Visante software are used. A regression line fitted to the data is shown (difference = $-0.11 + 0.34 \times \text{mean}$).

however, that there was a more fundamental problem. It might have been the case that the binary files used for the algorithm were different in image magnification or size than the image format used by the Visante software. To address this issue further, caliper measurements were simulated in Matlab within the same outline that was used for the automatic algorithm, i.e., a straight line was used to find the position of CBT1, CBT2, and CBT3. In this analysis, the simulated caliper measurements were taken within the same image file type used for algorithm measurements.

A Bland-Altman agreement analysis³¹ was conducted to compare the simulated calipers to the experienced examiner's calipers from the Visante software (Table 6). Although the mean of the differences at CBT3 was significantly different from 0, the magnitudes of all means of the differences were

small. In addition, the coefficients of repeatability when comparing the simulated calipers to the experienced examiner's calipers (Table 6) were comparable with the coefficients of repeatability when comparing the experienced and inexperienced examiners' calipers (Table 3).

DISCUSSION

As was discussed above, the ability of the Visante to image the ciliary muscle in a non-contact manner would be an important tool in studies that seek to provide insight into the development and function of the ciliary muscle throughout life, an area of research that has been previously neglected. Although, the Visante software is not currently set up to measure ciliary muscle images, the data presented above demonstrate that valid and repeatable measurements are possible. In the Visante, the geometric image distortion problems inherently associated with OCT,³⁴ appear to be corrected through hardware or software adaptations that occur before the generation of binary image files that can be exported from the instrument. An optical flat appeared as a flat image (Fig. 2). In addition, it was possible to register the axial scan depth of a Visante image of sclera and ciliary muscle tissue with a photograph of the same section of tissue using a single correction factor/refractive index, without additional adjustment for geometrical distortions. This indicates that the Visante is capable of imaging the length of the ciliary body without distorting the peripheral portions of the tissue. It also indicates that the binary files can be used for morphological assessments, and the researcher need only apply the appropriate refractive index for the tissue.

The semiautomatic algorithm outlined above is capable of outlining the ciliary body so that further morphological measurements can be made. In general, the measurements obtained from the algorithm were slightly larger (0.03 to 0.06 mm) than measurements made with the calipers in the Visante software. Because the algorithm chooses the vitreal/ciliary pigmented epithelium boundary based on pixel intensity and an examiner chooses caliper placement along this boundary based on his or her judgment, it is not surprising that minor differences would exist between an examiner's calipers and the semiautomatic algorithm.

The differences between the algorithm and the experienced examiner's calipers did not, however, appear to be because of differences in pixel intensity and examiner judgment alone. We suspected that there was a problem with the calipers cutting across the ciliary body in subjects with a more curved sclera (Fig. 1) before

TABLE 6.

Bland-Altman analyses of the agreement between the experienced examiner's caliper measurements of the ciliary body in the Visante software and calipers simulated within the outline created with the semiautomatic algorithm in Matlab (difference = simulated calipers – experienced examiner calipers)

Measurement (mm)	Mean of the differences	SD of the differences	95% Limits of agreement		Coefficient of repeatability
			Mean lower bound	Mean upper bound	
CBT1	0.02	0.12	-0.21	0.25	0.23
CBT2	-0.01	0.08	-0.17	0.16	0.16
CBT3	-0.02 ^a	0.06	-0.13	0.09	0.11

^at = -3.0, p = 0.006.

completing this study, but as Fig. 12 shows, the curvature of the sclera/ciliary body appears to be related to the thickness of the ciliary body. In subjects with a thicker ciliary body, the thickness measurements were larger when the semiautomatic algorithm followed the scleral curvature to find the location of the CBT3 measurement, and thinner when a straight-lined caliper was used to find the location because the straight-lined caliper located a more-posterior point. This has important implications for future studies. First, the problem does not appear to affect measurements closer to the sclera spur, so if researchers wanted or needed to use the Visante software's calipers for ciliary body thickness measurements, measurements such as CBT1 or CBTmax could be used. Second, if researchers did want or need to measure the more posterior portion of the ciliary body, the semiautomatic algorithm described in this report could be used to locate the measurement point by following the scleral curvature. A more posterior measurement might be more important in studies of how different portions of the ciliary body change during accommodation.

In addition to providing measurements of the ciliary body that generally agree well with Visante caliper measurements, the semiautomatic algorithm outlined in this report is acceptably repeatable. Within- and between-examiner variations in scleral spur selection represented a very small (6%) portion of the variance in the measurement when compared with the variance because of biological differences across subjects (80%). Any measurement of the ciliary body made with the semiautomatic algorithm should provide an ICC of 0.85 if researchers obtain three images of a subject's ciliary body and use the mean of the measurements. In an unpublished study, we were able to obtain six images of the ciliary body in first through fifth grade children during one testing session. Thus, we expect obtaining the three images required for this semiautomatic algorithm will be more than feasible in future studies of children.

A trend toward small differences was found in both the caliper and semiautomatic algorithm measurements when the first and last images from the measurements session were compared. Although the differences were not statistically significant after adjusting for multiple comparisons, the trend may indicate that the vertical alignment of the subjects may have slipped slightly during testing, resulting in a scanning position above or below the midpoint of the pupil by the time the last image was captured. Thus, when this vertical slippage occurred, it resulted in a significantly smaller thickness or cross-sectional area measurement in some cases. This highlights an important consideration during ciliary muscle imaging. Although a corneal reflex, i.e., a bright white line in the middle

of the image, provides a landmark for Visante measurements of the crystalline lens thickness,¹⁴ there is no such landmark to reference ciliary body imaging. The examiner must, therefore, carefully check subject alignment between images. Because only three images are needed in future studies that use the semiautomatic algorithm, rather than the six images obtained for this study, alignment may be easier to maintain. In addition, we are aware that the latest version of Visante software, Version 3.0, captures an image of the eye with a visible record of the scanning beam placement. This will allow postexamination evaluation of image capture. Images where the alignment of the eye is not at the mid-point of the pupil could be excluded from analysis, and this might reduce the variability in the measurement that is associated with image acquisition differences.

One of the limitations of this study, and a limitation of using the Visante for measurement of the ciliary body in general, is that the instrument is not capable of imaging the posterior zonules, which would serve as a marker for the posterior boundary of the ciliary muscle. Although a very recent article by Sheppard and Davies³⁵ reported the ability to visualize the "end" of the ciliary muscle, in our experience, many images do not have any visible endpoint. Thus, we have not reported on the length of the ciliary muscle in this report, because we have been unable to find a consistent marker for the posterior boundary of the ciliary body in these images. Even if there were a point where the ciliary muscle appeared to end in most images, Sheppard and Davies (2010) did not confirm that this was in fact the end of the muscle through histological analysis. Ciliary muscle length measurements may be important in presbyopia research, so in future studies of presbyopia concurrent imaging with UBM or magnetic resonance imaging would be required.

Another limitation of this imaging method is the need for further validation of the appropriate refractive index for the sclera and ciliary body. By imaging fixed human donor tissue, we have begun the process of this validation and obtained an estimate of $n = 1.56$. This estimate is probably artificially high because of the fixation of the tissue. Future studies are required to image fresh samples from multiple donors to refine this estimate in a manner similar to a recent report on the appropriate refractive index for the crystalline lens.³⁶ A direct comparison of Visante images of the sclera and ciliary body with UBM images would also be a useful future investigation into the appropriate refractive index, as long as the UBM is adjusted for the speed of sound through sclera.

Validity takes many forms, one of which is termed face validity, meaning that the test or measurement appears to measure what it

was intended to measure. In this laboratory, we have been able to find a relationship between Visante ciliary body thickness measurements and refractive error in children¹⁰ that is similar to other reports using UBM in adults.^{8,9} In addition, we have unpublished data of Visante ciliary body measurements in adults that also match these previous reports. Finally, we presented data at the 2009 American Academy of Optometry Annual Meeting demonstrating that measurements with this algorithm were capable of detecting changes in ciliary body thickness between the configuration of the ciliary muscle while resting and while accommodated to a four-dimensional stimulus in 25 adult subjects.³⁷ Certainly, further validation of the ciliary body measurements described in this report are required, but when we have used the algorithm measurements in several different types of studies, we have obtained values and results that are consistent with previous UBM studies.

The primary reason for imaging the donor sclera and ciliary body tissue was to determine the level of geometric and refractive distortions in the binary files we exported from the Visante. However, the exercise did provide some information about what the Visante can “see” in this area of the globe. In Fig. 5, it is apparent that only the ciliary muscle is visible and included in the measurements we have been calling ciliary body measurements. It is certainly advantageous to only view the ciliary muscle if that is what the research question requires, but the methods outlined in this report would not be suitable for research questions that required visualization of anything internal to the ciliary muscle. In the abstract for this report and in all future publications using this algorithm, we have described the thickness measurements obtained from Visante images as measurements of the ciliary muscle, rather than ciliary body measurements.

In summary, the semiautomatic algorithm for morphological measurement of the ciliary body that is outlined in this report is an acceptable measurement tool for future studies of the ciliary muscle. The algorithm is repeatable, requires only three images of the ciliary body for analysis, and agrees well with measurements obtained from the conventional Visante software. Additional features include providing masked and cross-sectional area measurements. Finally, it is capable of following the scleral curvature to accurately locate more posterior measurements of thickness and cross-sectional area.

APPENDICES

The appendices are available at <http://links.lww.com/OPX/A39> (A) and <http://links.lww.com/OPX/A40> (B).

ACKNOWLEDGMENTS

This research was supported by the National Science Foundation NSF DMS 0811003 and Sloan Fellowship (C-YK) and National Institutes of Health, National Eye Institute Grants R24-EY014792 (LTS), T32-EY013359 and K23EY019097 (KR), T35-EY07151 (LEG).

The research was supported by Award Number KL2 RR025754 (MDB) from the National Center for Research Resources, funded by the Office of the Director, National Institutes of Health (OD).

None of the authors have a commercial association with any products or instruments discussed in this manuscript.

The content is solely the responsibility of the authors and does not necessarily represent the official views of the National Center for Research Resources or the National Institutes of Health.

Received September 28, 2009; accepted September 14, 2010.

REFERENCES

1. Simpson ER. Ciliary body melanoma: a special challenge. *Can J Ophthalmol* 2004;39:365–71.
2. Mohamed MD, Gupta M, Parsons A, Rennie IG. Ultrasound biomicroscopy in the management of melanocytoma of the ciliary body with extrascleral extension. *Br J Ophthalmol* 2005;89:14–6.
3. Tran TA, Hirst LW, Axelsen RA, Welch R. Iris melanoma in 12-year-old boy. *Clin Experiment Ophthalmol* 2006;34:489–90.
4. Taban M, Sears JE, Singh AD. Ciliary body naevus. *Eye (Lond)* 2007;21:1528–30.
5. Croft MA, Kaufman PL. Accommodation and presbyopia: the ciliary neuromuscular view. *Ophthalmol Clin North Am* 2006;19:13–24.
6. Marchini G, Mora P, Pedrotti E, Manzotti F, Aldigeri R, Gandolfi SA. Functional assessment of two different accommodative intraocular lenses compared with a monofocal intraocular lens. *Ophthalmology* 2007;114:2038–43.
7. Marchini G, Ghilotti G, Bonadimani M, Babighian S. Effects of 0.005% latanoprost on ocular anterior structures and ciliary body thickness. *J Glaucoma* 2003;12:295–300.
8. Sheppard AL, Davies LN. In vivo analysis of ciliary muscle morphological changes with accommodation and axial ametropia. *Invest Ophthalmol Vis Sci* 2010;51:6882–9.
9. Muftuoglu O, Hosal BM, Zilelioglu G. Ciliary body thickness in unilateral high axial myopia. *Eye (Lond)* 2009;23:1176–81.
10. Bailey MD, Sinnott LT, Mutti DO. Ciliary body thickness and refractive error in children. *Invest Ophthalmol Vis Sci* 2008;49:4353–60.
11. Schultz KE, Sinnott LT, Mutti DO, Bailey MD. Accommodative fluctuations, lens tension, and ciliary body thickness in children. *Optom Vis Sci* 2009;86:677–84.
12. Pinero DP, Plaza AB, Alio JL. Anterior segment biometry with 2 imaging technologies: very-high-frequency ultrasound scanning versus optical coherence tomography. *J Cataract Refract Surg* 2008;34:95–102.
13. Dada T, Sihota R, Gadia R, Aggarwal A, Mandal S, Gupta V. Comparison of anterior segment optical coherence tomography and ultrasound biomicroscopy for assessment of the anterior segment. *J Cataract Refract Surg* 2007;33:837–40.
14. Lehman BM, Berntsen DA, Bailey MD, Zadnik K. Validation of optical coherence tomography-based crystalline lens thickness measurements in children. *Optom Vis Sci* 2009;86:181–7.
15. Westphal V, Rollins A, Radhakrishnan S, Izatt J. Correction of geometric and refractive image distortions in optical coherence tomography applying Fermat's principle. *Opt Express* 2002;10:397–404.
16. Kass M, Witkin A, Terzopoulos D. Snakes—active contour models. *Int J Comput Vis* 1987;1:321–31.
17. Cohen LD, Cohen I. Finite-element methods for active contour models and balloons for 2-D and 3-D images. *IEEE Trans Pattern Anal Mach Intell* 1993;15:1131–47.
18. Caselles V, Kimmel R, Sapiro G. Geodesic active contours. *Int J Comput Vis* 1997;22:61–79.
19. Xu C, Prince JL. Snakes, shapes, and gradient vector flow. *IEEE Trans Image Process* 1998;7:359–69.
20. Chan TF, Vese LA. Active contours without edges. *IEEE Trans Image Process* 2001;10:266–77.
21. Vese LA, Chan TF. A multiphase level set framework for image segmentation using the Mumford and Shah model. *Int J Comp Vis* 2002;50:271–93.
22. Li C, Kao C, Gore JC, Ding Z. Implicit active contours driven by

- local binary fitting energy. Proc IEEE Comput Soc Conf Comput Vis Pattern Recognit 2007;383014.
23. Li C, Kao CY, Gore JC, Ding Z. Minimization of region-scalable fitting energy for image segmentation. IEEE Trans Image Process 2008;17:1940–9.
 24. Myronenko A, Song X. Point set registration: coherent point drift. IEEE Trans Pattern Anal Mach Intell 2010;32:2262–75.
 25. Nemati B, Dunn A, Welch AJ, Rylander HG. Optical model for light distribution during transscleral cyclophotocoagulation. Appl Opt 1998;37:764–71.
 26. Nemati B, Rylander HG, Welch A. Optical properties of conjunctiva, sclera, and the ciliary body and their consequences for transscleral cyclophotocoagulation: erratum. Appl Opt 1997;36:416.
 27. Dirckx JJ, Kuypers LC, Decraemer WF. Refractive index of tissue measured with confocal microscopy. J Biomed Opt 2005;10:44014.
 28. Tearney GJ, Brezinski ME, Southern JF, Bouma BE, Hee MR, Fujimoto JG. Determination of the refractive index of highly scattering human tissue by optical coherence tomography. Opt Lett 1995;20:2258.
 29. Pardue MT, Sivak JG. Age-related changes in human ciliary muscle. Optom Vis Sci 2000;77:204–10.
 30. Tamm ER, Lutjen-Drecoll E. Ciliary body. Microsc Res Tech 1996;33:390–439.
 31. Bland JM, Altman DG. Statistical methods for assessing agreement between two methods of clinical measurement. Lancet 1986;1:307–10.
 32. Cox DR, Solomon PJ. Components of Variance. Boca Raton, FL: Chapman & Hall/CRC; 2003.
 33. Nunnally JC, Bernstein IH. Psychometric Theory, 3rd ed. New York: McGraw-Hill; 1994.
 34. Podoleanu A, Charalambous I, Plesea L, Dogariu A, Rosen R. Correction of distortions in optical coherence tomography imaging of the eye. Phys Med Biol 2004;49:1277–94.
 35. Sheppard AL, Davies LN. In vivo analysis of ciliary muscle morphological changes with accommodation and axial ametropia. Invest Ophthalmol Vis Sci 2010. (e-pub July 29, 2010).
 36. Uhlhorn SR, Borja D, Manns F, Parel JM. Refractive index measurement of the isolated crystalline lens using optical coherence tomography. Vision Res 2008;48:2732–8.
 37. Lossing LA, Richdale K, Sinnott LT, Bailey MD. Changes in ciliary body thickness with accommodation. Optom Vis Sci 2009;86: E-abstract 95815.

Melissa D. Bailey

*The Ohio State University College of Optometry
338 West Tenth Avenue
Columbus, Ohio 43210
e-mail: mbailey@optometry.osu.edu*